

A Dual-Layered Anode Buffer Layer Structure for All Solid-State Batteries

Yushi Lu,^{*[a, b]} Hansen Michael Chang,^[b] and Kai Peter Birke^[a]

Over the past few decades, lithium-ion batteries have garnered considerable attention, especially for their use in electric vehicles (EVs). In recent years, solid-state batteries have become increasingly popular due to their excellent safety features and potential for high energy density. However, solid-state batteries with lithium metal anodes present challenges in terms of electrochemical reactivity and cost. To address these challenges, alternative anode systems such as the “anode-free” approach are being explored. In this study, we introduced a dual-layered anode comprising a primary layer of physically vapor-deposited zinc and a secondary layer of carbon black, focusing on investigating the influence of varying thicknesses of the lithiophilic zinc layer on cell cycling performance. Among the three different zinc thicknesses chosen for this purpose –

categorized as thin (286 nm), medium (1.802 µm), and thick (6.519 µm) – the dual-layered anode buffer layer was analyzed in a single-layer full pouch cell. An in-depth investigation into the lithium-zinc alloying behavior was conducted through post-mortem analysis. From the results, we found that the combination of the zinc layer with the carbon black layer improved cell cycling performance in terms of discharge capacity retention compared to a single layer of either zinc or carbon black. The cycling performance of this dual-layered anode could be further enhanced by optimizing the zinc layer thickness, likely due to the irreversible alloying step of zinc and lithium. Among the various thicknesses evaluated, the thin zinc layer (286 nm) combined with the carbon black layer demonstrated the most promising cycling performance in all solid-state batteries.

Introduction

Lithium-ion batteries have gained significant interest over the past few decades, particularly for their application in electric vehicles (EVs). However, the use of liquid electrolytes in commercial lithium-ion batteries raises safety concerns due to the flammable nature of organic solvents.^[1–6] Simultaneously, the increasing demand for higher energy density in terms of both gravimetric and volumetric energy densities from the EV market has prompted extensive international research and development efforts in exploring and advancing the next generation of batteries with different chemistries. This encourages ongoing fundamental and applied research endeavors on a global scale..^[7]

Solid-state batteries have become increasingly popular in recent years due to their outstanding safety features and

potential for high energy density. However, it is important to be cautious when claiming that solid-state batteries have higher energy density than commercial liquid-based batteries. For example, when comparing batteries with the same cathode and anode materials (e.g. graphite, silicon anode) and similar operating conditions, solid-state batteries tend to have a slightly lower energy density (266 Wh/kg) compared to conventional batteries with liquid electrolytes (277 Wh/kg).^[8] This is primarily because solid-state electrolytes are denser than liquid electrolytes, which affects the overall energy density of the battery. In the case of lithium metal, it possesses a high specific capacity of 3860 mAh/g and an ultra-low negative potential of -3.040 V versus H^+/H_2 ,^[9] which could push the battery energy density onto the new era. Moreover, flammable liquid electrolyte is not favorable for combining with lithium metal due to its flammable nature, additionally, solid electrolytes are more compatible with lithium metal than flammable liquid electrolytes due to their non-flammable nature. Solid electrolytes also offer high mechanical strength, which has the potential to prevent the growth of lithium dendrites.^[10]

However, using lithium metal as the anode in all solid-state batteries is not cost-efficient. Ultra-thin lithium foil, less than 100 µm thick, costs over 1000 US\$/kg to manufacture.^[11] Moreover, lithium is highly reactive, making it challenging to handle in terms of materials processing and finding compatible cell chemistries. Recently, alternative anode systems like “anode-free” approach are being explored as feasible alternatives to lithium metal.

Figure 1 below shows the simplified working principle of “anode free” concept in all solid-state batteries during charging. During the charging step, the lithium ions are de-intercalated from the cathode active material, these lithium ions then move

[a] Y. Lu, Prof. Dr. K. P. Birke
University of Stuttgart
Institute for Photovoltaics (ipv):
Chair for Electrical Energy Storage Systems
Pfaffenwaldring 47, 70569, Stuttgart, Germany
E-mail: yushi.lu@mercedes-benz.com

[b] Y. Lu, Dr. H. M. Chang
Mercedes-Benz AG
Cell Technology1
Mercedes Benz Strasse 120, 70327, Stuttgart, Germany
E-mail: yushi.lu@mercedes-benz.com

Supporting information for this article is available on the WWW under <http://10.1002/batt.202400268>

© 2024 The Authors. *Batteries & Supercaps* published by Wiley-VCH GmbH. This is an open access article under the terms of the Creative Commons Attribution License, which permits use, distribution and reproduction in any medium, provided the original work is properly cited.

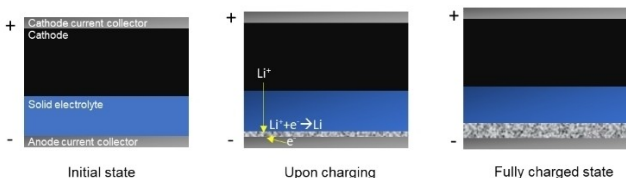


Figure 1. Working principle of “anode free” solid-state battery during charging.

through the solid electrolyte and eventually deposited onto the surface of the current collector located at the anode side, this results in a change in thickness on the anode side of approximately $4.8 \mu\text{m}$ due to lithium deposition, which corresponds to a charging capacity of $1 \text{ mAh} \cdot \text{cm}^{-2}$.^[12] However, the challenges experienced with the application of lithium metal in solid-state batteries will also arise in “anode free” configurations such as growth of lithium dendrites, unwanted decomposition as well as the influence of external pressure.^[12–14] Furthermore, the limited availability of lithium resources in the “anode-free” configuration remains a significant challenge in achieving long battery cycling life, lithium could be consumed due to the formation of SEI or dead lithium.^[15]

Many approaches have been demonstrated in the literature highlighting the importance of interfacial modification to enable homogeneous lithium plating and stripping. Organic coatings, such as PEO, PVDF, Li-PAA, and PDMS, improve interfacial contact due to their soft nature;^[16] however, their low ionic conductivity limits performance. Inorganic coatings, including lithiophilic metals (e.g., Ag, Zn, Mg) and their oxides, as well as ceramic Li^+ conductor materials, offer another viable solution for achieving stable cell cycling.^[17,18]

The all solid-state battery demonstrated by the research group from Samsung offers a practical and viable solution for sulfide-based solid-state batteries by incorporating a ultra-thin buffer layer (less than $10 \mu\text{m}$) of carbon-silver composite.^[19] Argyrodite sulfide was selected as the solid electrolyte due to its enhanced stability against lithium and high ionic conductivity. Additionally, a high-loading cathode ($6.8 \text{ mAh} \cdot \text{cm}^{-2}$) made of NCM was coated with $\text{Li}_2\text{O}-\text{ZrO}_2$ (LZO) to improve stability when in contact with the sulfide electrolyte. To further enhance lithium deposition and stripping reversibility during charging and discharging, the traditional Li^+ hosting structure at the anode side was replaced with an ultra-thin layer consisting of electronically conductive carbon black and lithiophilic silver nanoparticles. This change ensures a high level of reversibility in the lithium deposition and stripping processes.

The aforementioned battery demonstrated by Samsung research team showed excellent battery cycling performance, achieved in a pouch cell format (0.6 Ah) with coulombic efficiency of over 99.8% over 1000 cycles and incredible energy density of over $900 \text{ Wh} \cdot \text{L}^{-1}$.^[19] This invention demonstrates the potential to scale up sulfide-based solid electrolytes, making them suitable for electric vehicle (EV) applications by meeting the energy density and cycle life. The silver-carbon composite buffer layer offers a viable solution for lithium metal batteries, introducing the concept of “anode free” solid-state batteries. It

is important to note that the term “anode free” in this context does not imply the complete elimination of coating materials. Instead, it means that there is no traditional anode active material present, such as Li^+ host material or Li^+ lithiophilic material. Instead, an ultra-thin buffer layer coating is used solely as a buffer layer to facilitate uniform lithium deposition.

Following the significant increase in energy density, there has been a surge of interest in the field of “anode free” solid-state batteries, particularly in the study of the silver-carbon composite layer and other deposition-type anodes.

In 2021, the same research group published a paper showcasing the use of metal-carbon buffer layers with metals such as Zn, Al, Sn, Ni, and Ag.^[20] Among these metals, silver (Ag) still stood out as the most promising, exhibiting higher rate capability retention and discharge capacity retention over extended cycling periods. The research group highlights the crucial role of the carbon black layer, which electrochemically reduces lithium ions, facilitating their accumulation and over-saturation.

Nevertheless, there remain limitations to the practical application of the metal-carbon buffer layer. The expense of silver is a notable concern, and achieving a uniform distribution of silver nanoparticles within the carbon black matrix is challenging due to the nanoparticles’ tendency to aggregate. In this paper, we introduce a dual-layered approach consisting of a primary layer of physically vapor-deposited zinc and a secondary layer of carbon black with the following innovation highlights:

- (1) In comparison to silver, zinc is more abundant in the Earth’s crust and tends to be more cost-efficient. Additionally, zinc has the advantage of being soluble in lithium during the lithium deposition process and exhibits zero overpotential, making it a competitive material as lithiophilic seeds in “anode free” all solid-state batteries.^[21]
- (2) This dual-layered anode addresses the issue of metal particle agglomeration, offering a straightforward and scalable solution for anode-free solid-state battery design. Additionally, the complete coverage of the current collector with lithiophilic sites provided by the zinc layer enhances the homogeneity of lithium deposition, improving the cycling performance of solid-state battery.

Methods/Experimental Section

Preparation of Physical Vapor-Deposited Zinc Layer

The physical vapor deposition was conducted using a Cressington high vacuum sputter coater 208 HS. To generate samples of varying thicknesses, the sputtering time was adjusted while keeping other parameters constant. Three specific sputtering times were selected: 1 min and 7 s, 2 min and 15 s, 4 min and 30 s. These durations resulted in samples named Zn (thin), Zn (medium), and Zn (thick), respectively. The parameters adjusted for PVD are listed in Table 1 below:

Table 1. List of physical vapor deposition conditions.

Sample Name	Zn (thin)	Zn (medium)	Zn (thick)
Pumping time	30 min	30 min	30 min
Basic vacuum	1.5×10^{-5} mbar	1.5×10^{-5} mbar	1.5×10^{-5} mbar
Sputter pressure	2.2×10^{-3} mbar	2.2×10^{-3} mbar	2.2×10^{-3} mbar
Argon flux	18 sccm	18 sccm	18 sccm
Sputter parameter	0.7 kV, 80 mA	0.7 kV, 80 mA	0.7 kV, 80 mA
Sputtering time	1 min 7 s	2 min 15 s	4 min 30 s

Preparation of Carbon Black Layer

The conductive carbon black layer was fabricated through the wet coating technique. Imerys' carbon black C45 was selected alongside Kynar® HSV 1810 PVDF binder. The carbon black was maintained at a solid content ratio of 93:7 with the PVDF binder. The PVDF binder was pre-dissolved in NMP (N-Methyl-2-pyrrolidone) to have a solution with 10 wt% solid content. The slurry was prepared stepwise by adding NMP into the mixture of carbon black and PVDF solution, to ensure a uniform mixture, a Speed mixer was employed for multiple mixing steps, ensuring that the carbon black and PVDF binder was uniformly dispersed in the solvent. Subsequently, the final slurry was coated onto a 10 µm stainless steel current collector employing an Erichsen table coater. The wet-coated electrode sheets were initially dried on a heating plate set at 60 °C until visibly dry. Afterwards, the sheets were transferred to a vacuum drying oven for overnight drying at 80 °C.

Preparation of Dual-Layered Structure Anode

The dual-layered structure was fabricated as depicted in Figure 2 below. Other components were pre-cut to specific dimensions. For our standardized in-house pouch cell, the separator measures 2.5 cm by 2.5 cm, while the anode is 2.3 cm by 2.3 cm. In the initial step, the secondary layer consisting of carbon black was placed on top of the separator. Cold isostatic pressing (CIP) was employed to pre-press the two layers together under a pressure of 100 MPa for 10 min. However, upon releasing the pressure, the stainless steel current collector and the carbon black coating material exhibited poor adhesion, resulting in automatic detachment of the current collector from the carbon black coating. In the subsequent step, the physically vapor-deposited zinc with stainless steel substrate was aligned and stacked onto the separator with carbon black layer placed in between, a dual-layered anode consists of a primary layer of zinc and a secondary layer of carbon black stacked together with separator was prepared.

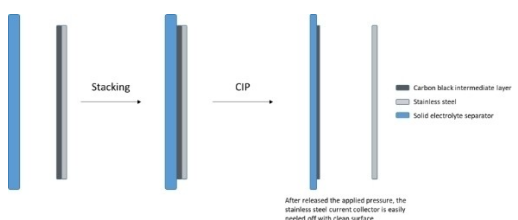


Figure 2. Procedure of transferring carbon black onto separator.

Preparation of Free-Standing Solid Separator

The production of the free-standing solid sulfide separator involved a wet coating method utilizing a table coater. This entire process was conducted within a glove box filled with argon with specific conditions: $\text{H}_2\text{O} < 0.1$ ppm, $\text{O}_2 < 0.1$ ppm. Binder HBNR was initially dissolved in a butyl acetate solvent at a concentration of 10 wt%. The weight ratio of the binder to argyrodite sulfide electrolyte powder ($\text{Li}_{5.5}\text{PS}_{4.5}\text{Cl}_{1.5}$) was 2 to 98. The appropriate quantities of the sulfide electrolyte powder, binder solution, and butyl acetate solvent were placed together in a plastic beaker along with ZrO_2 balls. This mixture was then mixed with thinky mixer to ensure a homogeneous slurry. Subsequently, the resulting slurry was ready for the coating process. A wet coating process was conducted using a table coater. A non-woven fabric sheet was positioned on an SiO_x -coated polyester film. This non-woven fabric sheet served as a support material for the production of the free-standing solid sulfide separator sheet. The slurry was then wet-coated onto the non-woven fabric sheet. The wet-coated sheets were first dried within the glove box at room temperature. Following this, they were transferred to a vacuum oven for additional drying overnight at 40 °C under vacuum conditions.

Preparation of Cathode

The production of the free-standing cathode electrode involved a drying coating process. The cathode active material, NCM523, was coated using a rotary vapor method with $\text{Li}_2\text{O}-\text{TiO}_2$ at a weight ratio of 0.5 mol% to prevent any undesired side reactions with the sulfide electrolyte. The $\text{Li}_2\text{O}-\text{TiO}_2$ -coated NCM523 cathode material was mixed with argyrodite sulfide electrolyte powder ($\text{Li}_{5.5}\text{PS}_{4.5}\text{Cl}_{1.5}$), polytetrafluoroethylene (PTFE) binder, and conductive carbon at a weight ratio of 80:17:1:2. The mixture was thoroughly blended manually with mortar and pestle until it formed a dough-like substance. The substance was further rolled with metal rolling pin at a heating plate with elevated temperature at 120 °C until the fully fabrilization of PTFE. This substance was then extruded using a calendar with a 100 µm gap to produce a dry cathode sheet. Finally, the dry cathode sheets were cut into pieces measuring 2.1 cm by 2.1 cm for use in cell assembly.

Single Layer Pouch Cell Assembly

The full cell assembly took place inside a glove box filled with argon with specific conditions: $\text{H}_2\text{O} < 0.1$ ppm, $\text{O}_2 < 0.1$ ppm. Battery components were carefully stacked and aligned together in the order of cathode current collector affixed with black thermoplastic polymer glue, the free-standing sulfide separator with one side conductive carbon coated facing anode direction, physically vapor-deposited zinc metal layer with stainless steel current collector, anode current collector affixed with black thermoplastic polymer glue.

Once the stacking was complete, the pouch cell was carefully lifted using tweezers and placed onto an impulse sealer for sealing three sides. The partially sealed pouch cell was subsequently affixed to an aluminum board for cold isostatic pressing (CIP), with a pouch bag serving to prevent oil contamination during the CIP process. This allowed the pouch cell to be pressed at a pressure of 500 MPa for 30 min. This high pressure ensured optimal interfacial contact, leading to reduced interfacial resistance. After the CIP step, the cell was returned to the glove box, and the opening side was sealed using a vacuum sealer.

The pressed pouch cell was equipped with stainless steel end plates at 2 MPa, ensuring uniform pressure distribution during the cell cycling process.

Morphology and Structural Characterization

Scanning electron microscopy (SEM) images of physically vapor-deposited samples were obtained with a Tescan Mira3 REM instrument, equipped with a field emission gun, operating at an accelerating voltage at 15 kV. The cross-section of physically vapor-deposited samples were prepared with an ion polisher. The SEM images of post-mortem analysis of cycled cells were obtained with a Zeiss Crossbeam 550 equipped with Oxford ultim Max 100 Energy dispersive X-ray (EDX) detector. The sample mounting and transferring to the electron microscope was realized under inert gas condition (nitrogen and argon). In order to avoid etching artefacts caused by the ion beam, a thin Pt-layer was deposited before the ion beam deposition.

X-ray diffraction (XRD) characterization was performed using a Rigaku MiniFlex 600 equipped with a CuK α source. In order to avoid the reaction of the sulfide and lithium with air, an air-tight sample holder was used to maintain the inert sample measurement

environment. XRD pattern was measured in the 2 θ range from 10°–90° at the speed of 10° per minute.

Electrochemical Characterization

The galvanostatic cycling was conducted using a BaSyTeC cycler in a climate chamber at a constant temperature of 60 °C. The pouch cell was equipped with end plates and subjected to a pressure of 2 MPa. Cycling was performed at either a 0.1 C charging rate and 0.2 C discharging rate for 100 cycles or a 0.5 C charging rate and 0.5 C discharging rate for 100 cycles, maintaining a cycling voltage window between 2.5 V and 4.25 V.

Results and Discussion

Figure 3A and 4B illustrate that with an increase in physical vapor deposition time from 1 minutes and 7 seconds to 2 minutes and 15 seconds, zinc crystals grains grew in terms of their size. However, when the PVD time was extended to 4 minutes and 30 seconds, irregular zinc deposition occurred, as shown in Figure 3C, filament-like structures were observed. This shows a change in the morphology of the zinc layer as deposition time increased. The measured average thickness of Zn (thin), Zn (medium), Zn (thick) are 286 nm, 1.802 μ m and 6.519 μ m, respectively.

To examine the effectiveness of the dual-layered approach, we prepared reference anodes with just carbon black and a pure Zn (thick) layer and prepared full cells in pouch cell format and cycled the cells galvanostatically.

The results, as shown in the Figure 4, indicated that both the pure single layer of carbon black and the Zn (thick) anode exhibited rapid capacity degradation. In contrast, a significant enhancement in cycling performance was evident in the dual-layered anode consisting of the aforementioned carbon black and Zn (thick) dual layers. The carbon black (CB) anode exhibited the lowest coulombic efficiency, approximately 94.5% over the last 10 cycles. However, the coulombic efficiency improved for the Zn (thick) anode, reaching around 98.1% over the last 10 cycles, and further improved for the ZnCB (thick) anode, achieving approximately 99.7% over the last 10 cycles.

When we examined the capacity retention for the first cycle, the pouch cells with ZnCB (thick), CB, and Zn (thick) exhibited capacities of 112.4 mAh·g⁻¹_{NCM}, 117.9 mAh·g⁻¹_{NCM}, and 132.2 mAh·g⁻¹_{NCM} respectively. Among these anodes, ZnCB (thick) demonstrated the poorest capacity retention at 112.4 mAh·g⁻¹_{NCM}. This could be attributed to a combination of irreversible Li⁺ deposition within carbon black layer and irreversible Li-Zn alloying process during the first charging step. It was worth noting that carbon black itself could serve as an anode buffer layer for cycling, it could allow Li⁺ deposition within its structure. Once the CB layer can no longer host in-situ deposited lithium, it begins to deposit between the saturated carbon black layer and the current collector.^[20] From our experiments, we noted that full pouch cells with pure carbon black anode underwent rapid capacity degradation over 100 cycles, this could be caused by the irregular deposition of lithium within the carbon black matrix, leading to the formation

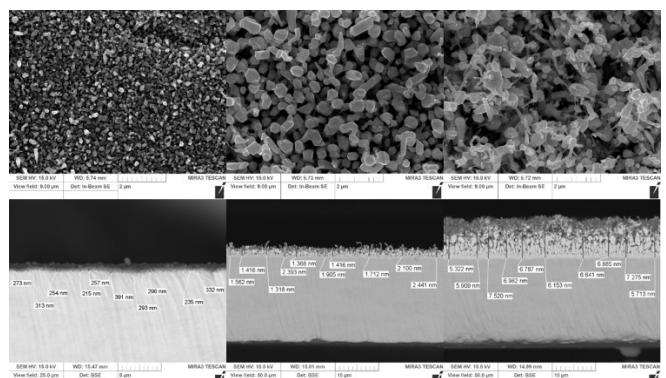


Figure 3. Topography of physically vapor-deposited zinc on stainless steel current collector with: (A) zinc (thin); (B) zinc (medium); (C) zinc (thick), cross-sectional SEM images of PVD zinc on SUS current collector with (D) zinc (thin); (E) zinc (medium); (F) zinc (thick).

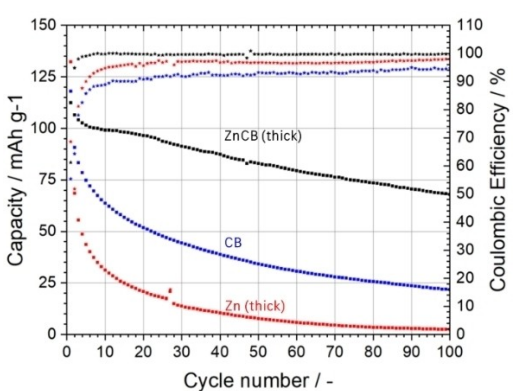


Figure 4. Capacity retention and coulombic efficiency of all solid-state batteries with different anodes: thick physically vapor-deposited zinc anode was named as Zn (thick) (red), carbon black anode was named as CB (blue), dual-layer anode consisted of physically vapor-deposited thick zinc and carbon black was named as ZnCB (thick) (black). The pouch cells were cycled at C-rate of 0.1 C charging/0.2 C discharging at 60 °C under 2 MPa.

of “dead lithium”. The cycling performance of the anode composed solely of a PVD zinc layer was also notably poor. This could be attributed to either an unstable interface between the sulfide electrolyte and the Li–Zn alloy or the limited rate of lithium diffusion within the zinc layer at this specific C-rate (0.1 C charging/0.2 C discharging). When carbon black and the zinc layer were combined, the overall cycling performance was improved.

Dual-layered anodes with varying thicknesses of the zinc layers were prepared, and these cells were designated as ZnCB (thick), ZnCB (medium), and ZnCB (thin), in this context, “thick,” “medium” and “thin” refer to the thickness of the PVD zinc layer. They were initially tested at a C-rate of 0.1 C charging and 0.2 C discharging (as shown in Figure 5A), and subsequently at a higher C-rate of 0.5 C charging and 0.5 C discharging (as shown in Figure 5B).

The first-cycle discharge capacities for anodes with different zinc thicknesses aligned with our previous assumption that the irreversible Li–Zn alloying during the first charging step, and the so-caused discharge capacity loss was proportionate to the amount of zinc used in the dual-layered anode. Specifically, at the C-rate of 0.1 C charging and 0.2 C discharging, the first-cycle discharge capacities for anodes ZnCB (thin), ZnCB (medium), and ZnCB (thick) were $147.9 \text{ mAh} \cdot \text{g}^{-1}_{\text{NCM}}$, $138.7 \text{ mAh} \cdot \text{g}^{-1}_{\text{NCM}}$, and $112.4 \text{ mAh} \cdot \text{g}^{-1}_{\text{NCM}}$, respectively. At the C-rate of 0.5 C charging and 0.5 C discharging, the first-cycle discharge capacities for anodes ZnCB (thin), ZnCB (medium), and ZnCB (thick) were $123.4 \text{ mAh} \cdot \text{g}^{-1}_{\text{NCM}}$, $116.8 \text{ mAh} \cdot \text{g}^{-1}_{\text{NCM}}$, and $75.6 \text{ mAh} \cdot \text{g}^{-1}_{\text{NCM}}$, respectively. During low C-rate testing, the capacity retention followed the same trend of decreasing capacity from the 10th cycle onwards. This indicates that the main reason for capacity degradation is likely associated with the quality of other battery components, such as non-optimized cathode composition. Alternatively, it could result from stresses induced by the thickness change in the anode, leading to accelerated degradation of the cathode active material.^[22]

On the other hand, with higher C-rate testing, differences in capacity retention among different anodes became more apparent. In the case of the ZnCB (thick) anode, during first three cycles, the capacity dropped from an initial capacity of

$75.6 \text{ mAh} \cdot \text{g}^{-1}_{\text{NCM}}$ to $49.1 \text{ mAh} \cdot \text{g}^{-1}_{\text{NCM}}$. This could be attributed to the limited Li⁺ diffusion rate within the thick zinc layer, resulting in continuous capacity loss during first three cycles.

The study of different Zn anode thicknesses showed that the ZnCB (thin) anode performed the best, outperforming other thicker zinc layer anodes. This was inspiring because thinner anodes could potentially lead to higher overall energy density in batteries. In our work, we used a dual-layered anode with a primary zinc layer around 286 nm thick and a secondary layer of carbon black around 3 μm thick. This setup allowed the solid-state battery to function with decent capacity retention, which pointed out a practical step towards realizing the “anode-free” concept for all solid-state batteries.

To gain a deeper understanding of carbon intercalation and alloying behavior, differential capacity (dQ/dV) curves for various anodes were generated for the 1st, 2nd, and 3rd cycles, as depicted in the Figure 6. The investigation included pure zinc anodes with distinct thicknesses labeled as Zn (thick), Zn (medium), and Zn (thin), along with dual-layered anodes labeled as ZnCB (thick), ZnCB (medium), and ZnCB (thin).

In the dQ/dV curves, distinct observations emerged. For the Zn (thick) anode (Figure 6A), during the initial charging step, the oxidative reaction occurred at approximately 3.4 V, followed by a series of overlapped oxidative peaks. This occurrence could be attributed to irreversible Li–Zn alloying. In the case of the Zn (medium) anode (Figure 6C), similar alloying peaks occurred around 3.4 V, although less prominently than in Zn (thick). These alloying peaks vanished from approximately 3.6 V onward, indicating the conclusion of the alloying process. The lower intensity peaks of Figure 6C is likely due to the smaller quantity of zinc in the Zn (medium) anode, which participated in the alloying phase. This trend was further confirmed by the Zn (thin) anode (Figure 6E). This finding further explained the lowest discharge capacity at 1st cycle for Zn (thick) among the three anodes with different zinc thicknesses; Zn (thick) consumed the most lithium in the system. Furthermore, in the subsequent cycles, these alloying peaks disappeared, indicating the irreversible nature of the alloying behavior.

Upon adding a secondary layer of carbon black between various thickness zinc layers and the solid electrolyte layer, the

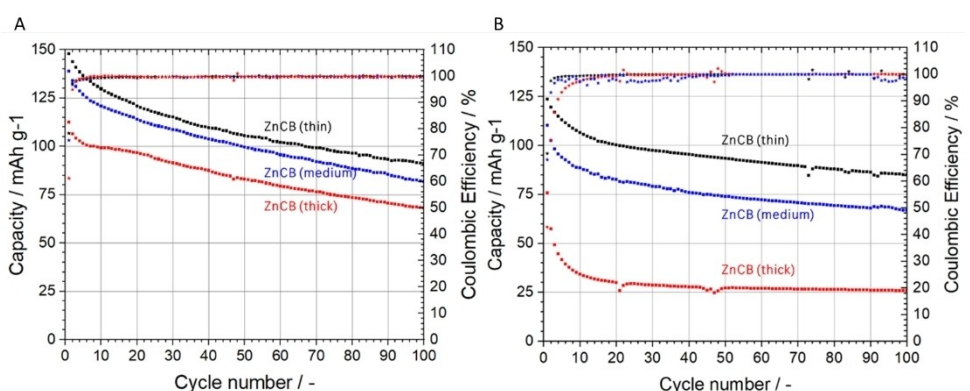


Figure 5. Capacity retention and coulombic efficiency of all solid-state batteries with different anodes: (A) full pouch cells were cycled under 0.1 C/0.2 C charge/discharge C-rate at 60°C under 2 MPa; (B) full pouch cells were cycled under 0.5 C/0.5 C charge/discharge C-rate at 60°C under 2 MPa.

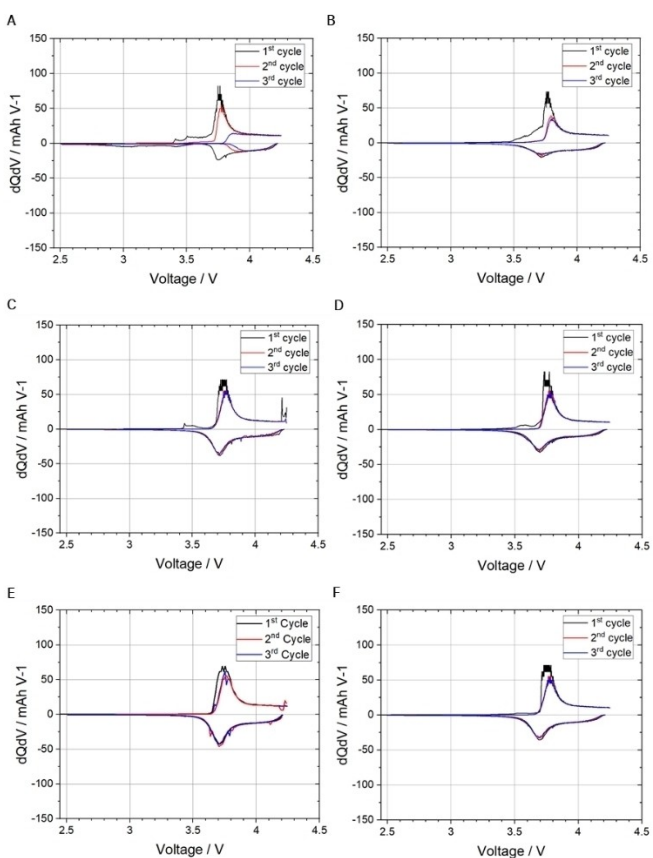


Figure 6. Differential capacity (dQ/dV) plots of the 1st, 2nd, and 3rd charging/discharging curves of different anodes: (A) Zn (thick); (B) ZnCB (thick); (C) Zn (medium); (D) ZnCB (medium); (E) Zn (thin); (F) ZnCB (thin).

alloying behavior was still observed in all dual-layered anodes. However, the alloying transpired at a higher voltage, roughly 3.5 V. The occurrence of a series of overlapped oxidative peaks as it was noted in the pure zinc anodes persisted in the dual-layered anodes. In the case of ZnCB (medium) (Figure 6D) and ZnCB (thin) (Figure 6F), alloying tended to terminate prior to the occurrence of characteristic peaks related to cathode active material phase transformation. Moreover, the intensity of the alloying peak diminished. Nevertheless, the dQ/dV plot did not exhibit an oxidative peak linked to carbon intercalation. This likely resulted from the limited amount of carbon used in the dual-layered structure.

However, among all the anodes depicted in Figure 6, the oxidative peaks associated with alloying behavior were only evident during the initial charging cycle and disappeared in subsequent charging cycles. This disappearance suggested the irreversibility of the Li–Zn alloying process. To substantiate this assertion, post-mortem analysis was conducted to gain insights into chemical changes within a cycled cell.

To gain insight into lithium deposition within the dual-layered anode and to investigate morphological changes, two cells were taken apart at 100% state of charge (SOC) and 0% state of charge (SOC), respectively. Delamination happened during teardown due to the bad adhesion within the carbon black layer, resulting in two distinct parts. One part contained

the stainless steel current collector and with the zinc layer, with possibly residual carbon black on top, and the other part comprised the bulk of the carbon black, separator, and cathode underneath. These two segments were named as “Anode (SUS)” and “Anode (SE)” for further clarity, as shown in Figure 7, “SUS” stands for stainless steel current collector, “SE” stands for solid electrolyte.

The top view of these two segments was depicted in Figure 8. Upon examination, in the case of the anode (100% SoC), no evident lithium dendrites were observed. Instead, different lithium deposition morphologies within various matrix materials were identified. In the Anode (SUS) sample (Figure 8A), the alloying of lithium and zinc impeded the formation of lithium dendrites. The Zn–Li alloy maintained a morphology similar to that of zinc, albeit with an expanded volume with continuous phase. Conversely, in the Anode (SE) sample (Figure 8B), lithium deposition occurred in filament-like shapes within the carbon black matrix. This could potentially result in the development of lithium dendrites in the absence of an underlying alloying layer. In the case of the anode at 0% SoC, the anode (SE) (Figure 8D) exhibited an amorphous morphology unlike the filament-like structure observed previously, presenting the delithiated state of carbon black.

To better differentiate between zinc and carbon and potentially locate the lithium, we conducted elemental mapping using Energy Dispersive X-ray (EDX) for N, Zn, C, S, and N as shown in Figure 9. The samples were exposed to nitrogen

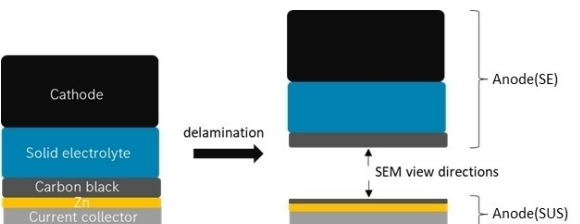


Figure 7. Sketch of sample preparation for post-mortem analysis.

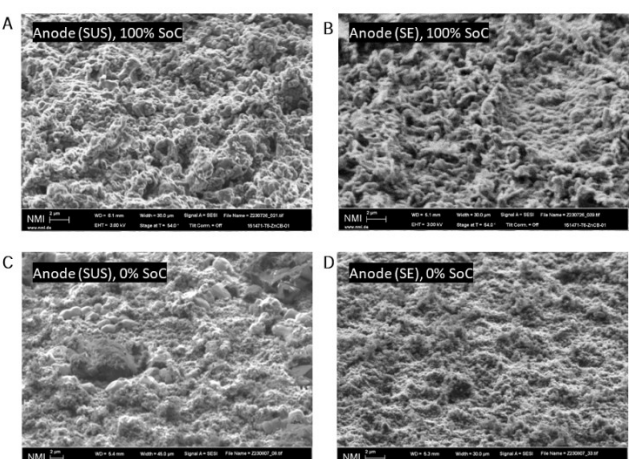


Figure 8. The scanning electron microscopy (SEM) images of: (A) Anode (SUS), taken apart at 100% SoC; (B) Anode (SE), taken apart at 100% SoC; (C) Anode (SUS), taken apart from 0% SoC; (D) Anode (SE), taken apart at 0% SoC, respectively.

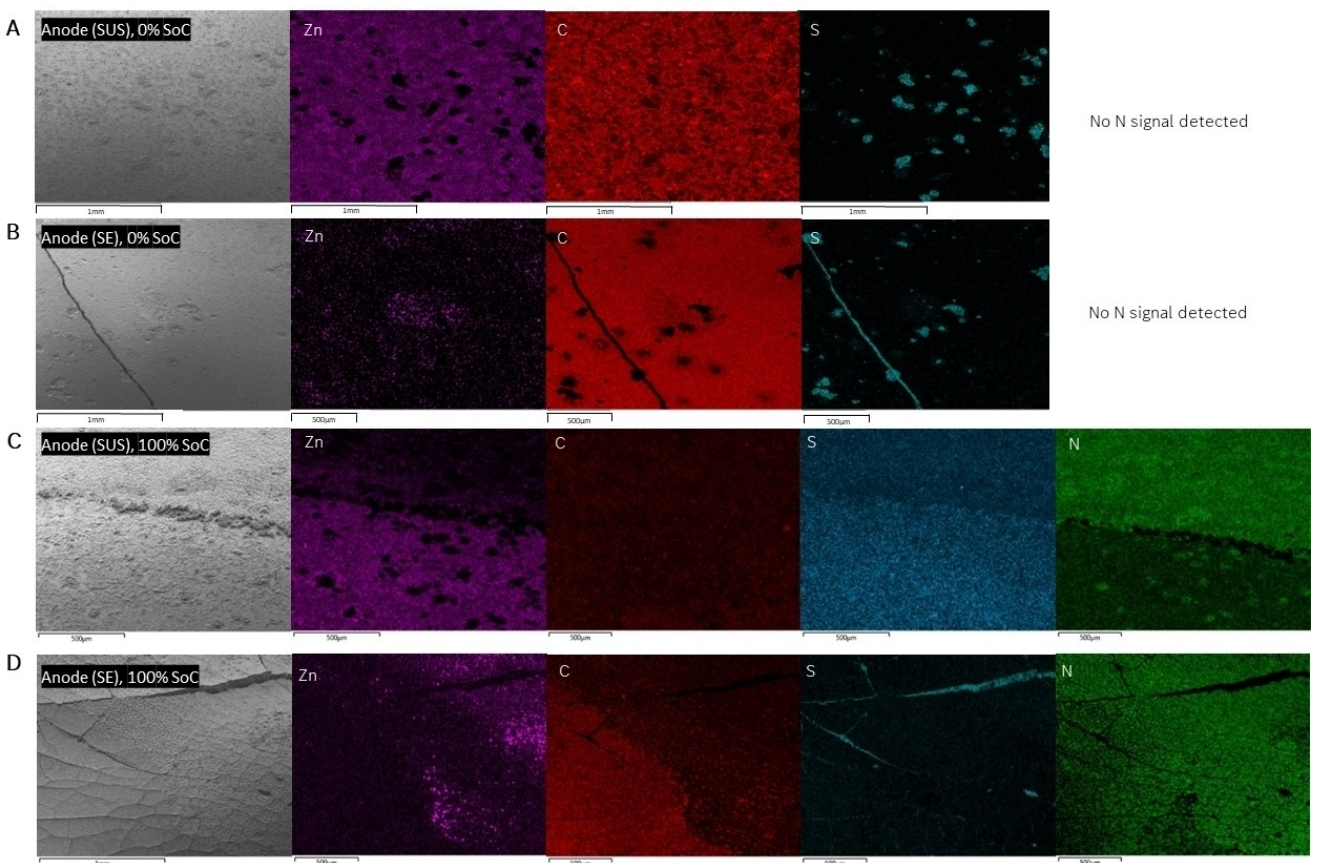


Figure 9. SEM images with energy dispersive X-ray (EDX) mapping analysis of different anode samples: samples were shortly exposed to nitrogen during the transferring chamber; therefore, the elemental area mapping of N indicates the area mapping of Li due to the reactivity of nitrogen and lithium.

during sample transfer for SEM measurement. Due to the fact that metallic lithium reacts rapidly with nitrogen to form lithium nitride (Li_3N), we used the mapping of the nitrogen element to identify the lithium domains.

In the case of the anode taken apart from a cell at 0% State of Charge (SoC), there was no nitrogen signal detected (seen in Figure 9AB). This indicates that no metallic lithium remained after the cell was fully discharged. Carbon was detected in both the anode (SUS) and anode (SE) samples, suggesting that the anode was taken apart from the carbon black layer with the lowest adhesion.

For the anode samples taken from a cell at 100% SoC (seen in Figure 9CD), we were able to detect nitrogen signals in both anode (SUS) and anode (SE). When comparing the nitrogen and zinc elemental mapping for the Anode (SUS) sample (Figure 9C), nitrogen was detected in areas where the zinc signal was quite low. This suggested that the in-situ deposited lithium covered the PVD zinc layer, likely due to excessive lithium deposition. The same trend was observed for anode (SE) (Figure 9D), where nitrogen-rich areas showed less carbon signal, indicating that the in-situ deposited lithium was located underneath the carbon black layer, which means the lithium was in-situ deposited in between the carbon layer and the zinc layer. However, there was also evidence of lithium deposition in the

carbon layer, as areas with strong carbon signals still showed clear nitrogen signals.

To gain a more comprehensive understanding of lithium deposition within the depths of both Anode (SUS) and Anode (SE), cross-sections of these two samples were meticulously prepared using a focused ion beam (FIB) technique. The FIB was directed from the surface of each sample, going through anode materials.

Regarding the Anode (SUS) sample taken apart from a full charged cell (100% SoC), seen in Figure 10A, due to a substantial amount of physically vapor-deposited zinc, the alloying initiated on the surface of the zinc layer and then progressed throughout its thickness, resulting in a phase separation where there was a Li-rich area and a Zn-rich area. A crucial point to consider was that lithium remained undetectable using SEM-EDX characterization, and Li-Zn alloy significantly reduced the chemical reactivity of lithium. In this case, the reactivity of lithium and nitrogen was greatly diminished. Consequently, we were unable to definitively determine the composition of the Zn-rich area, whether it consisted of pure zinc or Li-Zn alloy. In the case of the Anode (SE) sample, seen in Figure 10B, nitrogen was detected on the surface of the carbon black, this observation supported the notion that lithium deposition took place beneath the carbon black layer, which was consistent with findings from previous literature.^[19,20]

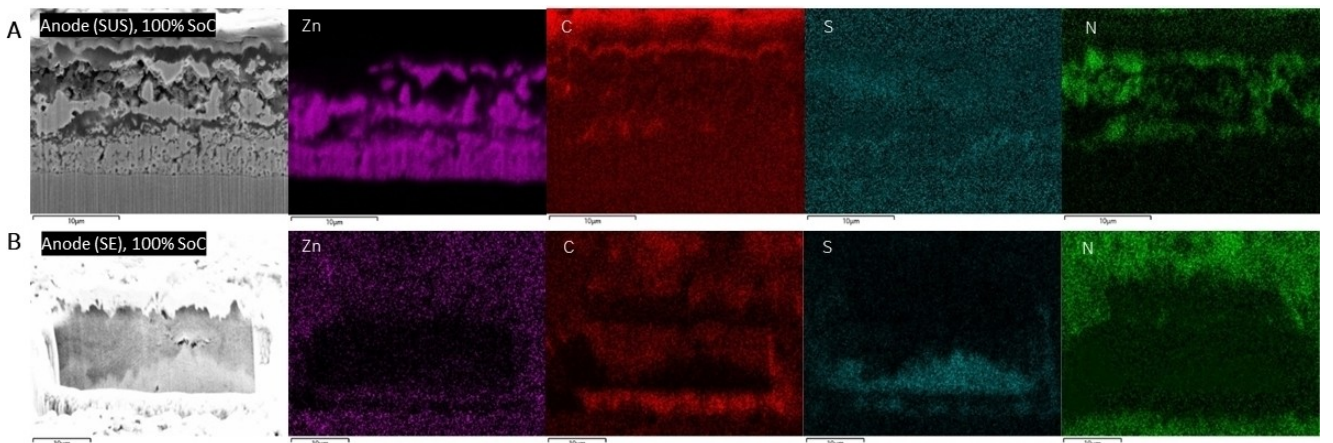


Figure 10. Cross-sectional SEM images of dual-layer anodes: (A) Anode (SUS) at fully charged state; (B) Anode (SE) at fully charged state with EDS mapping analysis of elements such as Zn, C, S and N.

Additionally, the presence of zinc element was predominantly observed on the carbon black surface. This zinc residue might originate from the anode delamination process. Due to the limitations of this characterization technique, it was not possible to detect the presence of Li–C composite or the formation of Li–Zn alloy.

The second anode sample was extracted from a fully discharged cell (0% SoC). As shown in Figure 11A, the zinc layer retained its integrity after full discharge, but it exhibited increased thickness and reduced porosity compared to the pristine zinc layer (seen in Figure 3). This change could be attributed to the presence of remaining lithium within the Li–Zn alloy. There was also an observed thickness reduction in the carbon black layer in the fully discharged cell (seen in Figure 11B) when it was compared to the fully charged state (seen in Figure 10B). However, it was important to note that this observation was limited in its conclusiveness due to the uneven thickness of the carbon layer in a compressed state.

According to our post-mortem analysis, we observed the deposition of lithium beneath the layer of carbon black, along with its alloying with the zinc layer. When discharging the battery to a fully discharged state, the elemental lithium that was deposited in-situ was removed. However, we also noticed a reduction in capacity due to an increased amount of zinc in Figure 5 and an irreversible alloying peak in the first charging cycle as shown in Figure 6, which further enhanced our previous conclusion that an irreversible alloying process occurred during the initial charging cycle, and it was associated with the alloying behavior of lithium and zinc.

To better understand the structural changes in the dual-layered anode at fully charged and fully discharged states, we conducted X-Ray Diffraction (XRD) measurements on the fully charged Anode (SE) and Anode (SUS), together with fully discharged Anode (SE) and Anode (SUS). In Figure 12A, the peaks associated with the LiZn alloy were highlighted. Unfortunately, due to the limitations of X-Ray diffraction, we were unable to observe the in-situ deposited lithium. However, we

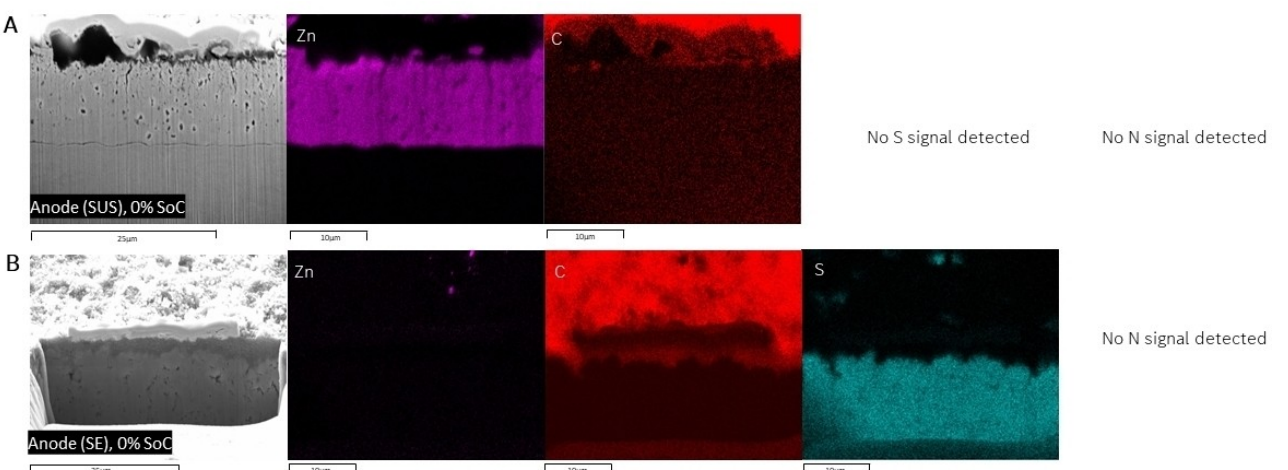


Figure 11. Cross-sectional SEM images of dual-layer anodes: (A) Anode (SUS) at fully discharged state; (B) Anode (SE) at fully discharged state with EDS mapping analysis of elements such as Zn, C, S and N.

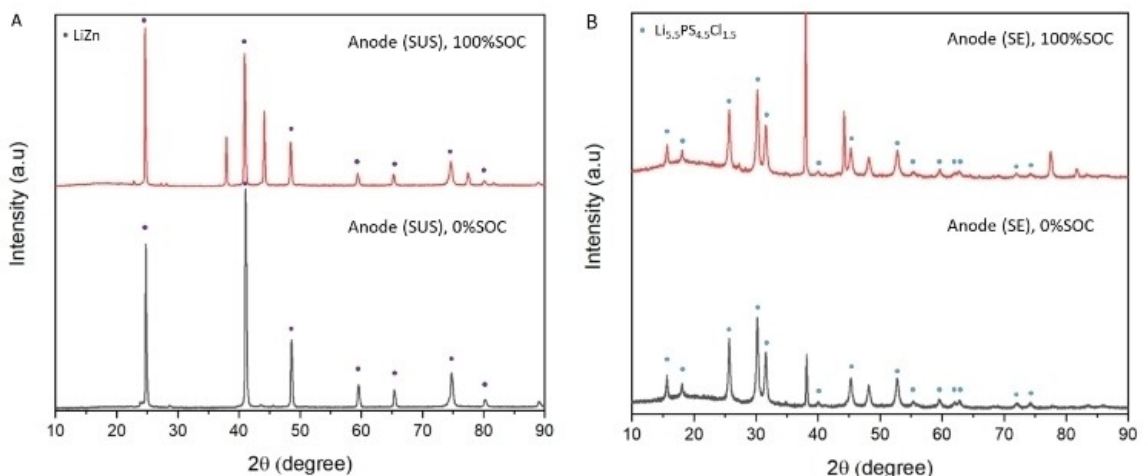


Figure 12. XRD pattern of: (A) Anode (SUS) at fully charged state (100% SOC) and fully discharged state (0% SOC); (B) Anode (CB) at fully charged state (100% SOC) and fully discharged state (0% SOC).

did find its alloy form, LiZn, in both fully charged and discharged Anode (SUS) samples. This confirmed the presence of alloy at the fully discharged state, indicating an irreversible lithium alloying step.

Based on the post-mortem analysis, we proposed the following working mechanism schematic, illustrated in Figure 13. Upon charging, lithium saturates the carbon layer initially. As saturation continues, lithium-zinc alloying occurs at the interface between the carbon black and the zinc layer. With further charging, metallic lithium is deposited between the fully alloyed zinc layer and the fully saturated carbon black layer. During discharge, the process reverses: metallic lithium is stripped first, followed by de-alloying and then de-saturation of the carbon black layer. However, the de-alloying step is not fully reversible during the first cycle, resulting in the zinc layer

remaining as a Zn–Li alloy rather than reverting to pure zinc after full discharge.

Conclusions

In this study, we introduced a dual-layered anode consisting of a primary layer of physically vapor-deposited zinc and a secondary layer of carbon black. This combination of lithophilic zinc and highly electronically conductive carbon black greatly improved the cycling performance of solid-state batteries. We explored the impact of the zinc layer with three different thicknesses. Notably, the ultra-thin zinc coating, approximately 286 nm thick, exhibited the best performance with the least capacity loss during the first cycle. This suggested an irreversible alloying of lithium and zinc, a conclusion supported by

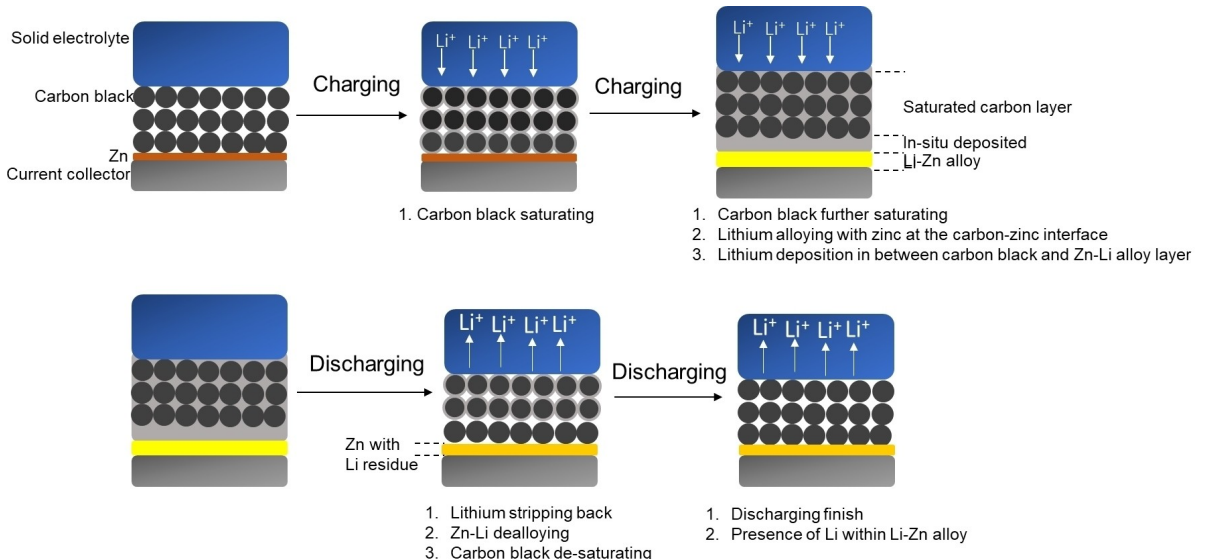


Figure 13. Proposed working mechanism schematic of a dual-layered anode all solid-state battery during charging and discharging.

XRD results. Additionally, at a high charging and discharging rate (0.5 C), the dual-layered anode with a thick zinc layer (6.519 µm) showed rapid capacity fading. This implies the presence of an additional Li⁺ diffusion mechanism within the thick zinc layer, limiting the lithophilic seeding effect of zinc.

Indeed, there are several other aspects to explore in the development of deposition-type anodes with a dual-layered structure. These include investigating the optimal thickness of the carbon black layer and exploring alternative lithophilic metals. This research offers valuable insights into the design of anodes for solid-state batteries, particularly in the context of the “anode-free” concept. It opens the door to further advancements in the field of solid-state battery technology.

Supporting Information

Supporting information for this article is available.

Acknowledgements

The financial support from Mercedes-Benz AG greatly contributed to the successful completion of this project. We thank Dr. Steffen Hink and Mahir Uenal for providing us with the cathode and separator materials to make this research possible. We also thank Clementine Warres from Natural and Medical Sciences Institute (NMI) for her assistance with the cross-section characterization. Open Access funding enabled and organized by Projekt DEAL.

Conflict of Interest

The authors declare no conflict of interest.

Keywords: Solid-state battery · anode free · lithophilic alloy · interfacial modification

- [1] Y. Duan, X. Bai, T. Yu, Y. Rong, Y. Wu, X. Wang, J. Yang, J. Wang, *J. Energy Storage* **2022**, *55*, 105382.
- [2] Z. A. Ghazi, Z. Sun, C. Sun, F. Qi, B. An, F. Li, H.-M. Cheng, *Small (Weinheim an der Bergstrasse, Germany)* **2019**, *15*, e1900687.
- [3] W. Li, Y. Pang, J. Liu, G. Liu, Y. Wang, Y. Xia, *RSC Adv.* **2017**, *7*, 23494.
- [4] J. Liang, J. Luo, Q. Sun, X. Yang, R. Li, X. Sun, *Energy Storage Mater.* **2019**, *21*, 308.
- [5] H. Shen, E. Yi, L. Cheng, M. Amores, G. Chen, S. W. Sofie, M. M. Doeff, *Sustain. Energy Fuels* **2019**, *3*, 1647.
- [6] N. Suzuki, T. Watanabe, S. Fujiki, Y. Aihara, *Advanced Energy and Sustainability Research* **2011**, *2*(11), 2100066.
- [7] C. P. Grey, D. S. Hall, *Nat. Commun.* **2020**, *11*, 6279.
- [8] C. Heubner, S. Maletti, H. Auer, J. Hüttl, K. Voigt, O. Lohrberg, K. Nikolowski, M. Partsch, A. Michaelis, *Adv Funct Materials* **2021**, *31*, 2106608.
- [9] Y. Lu, C.-Z. Zhao, H. Yuan, X.-B. Cheng, J.-Q. Huang, Q. Zhang, *Adv Funct Materials* **2021**, *31*, 2009925.
- [10] D. Cao, X. Sun, Q. Li, A. Natan, P. Xiang, H. Zhu, *Matter* **2020**, *3*, 57.
- [11] R. Schmuck, R. Wagner, G. Hörpel, T. Placke, M. Winter, *Nat. Energy* **2018**, *3*, 267.
- [12] G. Whang, Q. Yan, D. Li, Z. Wei, D. Butts, P. Sautet, J. Luo, B. Dunn, *J. Mater. Res.* **2021**, *36*, 797.
- [13] J. Kasemchainan, S. Zekoll, D. Spencer Jolly, Z. Ning, G. O. Hartley, J. Marrow, P. G. Bruce, *Nat. Mater.* **2019**, *18*, 1105.
- [14] T. Famprakis, P. Canepa, J. A. Dawson, M. S. Islam, C. Masquelier, *Nat. Mater.* **2019**, *18*, 1278.
- [15] Z. Xie, Z. Wu, X. An, X. Yue, J. Wang, A. Abudula, G. Guan, *Energy Storage Mater.* **2020**, *32*, 386.
- [16] C. Guo, Y. Shen, P. Mao, K. Liao, M. Du, R. Ran, W. Zhou, Z. Shao, *Adv Funct Materials* **2023**, *33*(10), 2213443.
- [17] M. Du, Y. Sun, B. Liu, B. Chen, K. Liao, R. Ran, R. Cai, W. Zhou, Z. Shao, *Adv Funct Materials* **2021**, *31*(31), 2101556.
- [18] M. Du, K. Liao, Q. Lu, Z. Shao, *Energy Environ. Sci.* **2019**, *12*, 1780.
- [19] Y.-G. Lee, S. Fujiki, C. Jung, N. Suzuki, N. Yashiro, R. Omoda, D.-S. Ko, T. Shiratsuchi, T. Sugimoto, S. Ryu, J. H. Ku, T. Watanabe, Y. Park, Y. Aihara, D. Im, I. T. Han, *Nat. Energy* **2020**, *5*, 299.
- [20] N. Suzuki, N. Yashiro, S. Fujiki, R. Omoda, T. Shiratsuchi, T. Watanabe, Y. Aihara, *Adv Energy Sustain Res* **2021**, *2*, 2100066.
- [21] K. Yan, Z. Lu, H.-W. Lee, F. Xiong, P.-C. Hsu, Y. Li, J. Zhao, S. Chu, Y. Cui, *Nat. Energy* **2016**, *1*.
- [22] J. Kang, H. R. Shin, J. Yun, S. Kim, B. Kim, K. Lee, Y. Lim, J.-W. Lee, *Energy Storage Mater.* **2023**, *63*.

Manuscript received: April 20, 2024
Accepted manuscript online: June 15, 2024
Version of record online: August 4, 2024